Large Eddy Simulation of a Swirling Non-Premixed Flame

H. El-Asrag[*]and S.Menon[†]

School of Aerospace Engineering

Georgia Institute of Technology

Atlanta, Georgia 30332

hossam_el-asrag@ae.gatech.edu, suresh.menon@ae.gatech.edu

Large-Eddy Simulations (LES) using a subgrid mixing and combustion model based on the linear-eddy mixing (LEM) approach are carried out to study a highly swirling non-premixed flame in a realistic combustor configuration. Detailed measurements obtained for this configuration are compared to the LES predicted flow field. Both non-reacting mixing and reacting cases are simulated, and very good agreement is obtained for nearly all the properties compared. In particular, very good agreement is obtained for both the mean and the fluctuation velocity profiles in both cold and reacting cases. Additional properties, such as, the recirculation zone size and its location, the flame structure and its length are all captured accurately as well. These results confirm the ability of the LEMLES approach developed for simulating turbulent reacting flows.

I.   Introduction

LES has been applied to many non-reacting and reacting flow cases with reasonable success in recent studies.[1, 2, 3, 4] Validation of the LES approach is essential to establish its reliability and to afford confidence when new configurations have to be simulated. Over the last few years, we have been systematically evaluating the ability of a new subgrid mixing and combustion model for LES application (LEMLES, discussed later) for generalized application to combustion in realistic combustors without requiring any ad hoc model adjustments. Past studies have demonstrated the ability of this model for scalar mixing,[2, 5, 6] premixed combustion[7, 8, 9, 10] and spray combustion.[11, 12] In most cases, the test configurations chosen for validation were operating close the conditions observed in realistic gas turbine engines. Here, experimental data[13, 14] obtained at Sandia National Laboratories (SNL) are utilized to study and validate our LEMLES approach for a highly swirl non-premixed combustion flow. We chose this configuration and test condition since they closely represent the flow characteristics observed in gas turbine engines. In particular, swirling flow is employed in all gas turbine engines to achieve aerodynamic flame stabilization, and validation in such a flow will further establish the LESLEM capability for non-premixed combustion applications.

The SM1 flame[13, 14] is chosen as a test case for the current study. A non-reacting case close to this flame is also simulated. All the velocity field components, as well as the temperature and some species are available in the data base and therefore, can be used for direct comparison. We believe that this study is the first reported LES attempt of this swirling bluff body flame.

This paper is organized as follows. In the next section, we describe (albeit briefly) the mathematical formulation and the subgrid closure. This is followed by the configuration set up in Section III, and then, results for the non-reacting and reacting studies are reported in Sections IV and V. Finally, in Section VI we conclude this study and note some future research issues.

---

[*]Graduate Research Assistant, AIAA Student Member

[†]Professor, AIAA Associate Fellow

II.   Mathematical Formulation

In this paper, the full multi-species, compressible Navier Stokes equations are solved in the strong conservative form. The fluid is assumed Newtonian with no body forces and in single phase. The LES equations are derived by using spatial Favre filtering.[15] The final LES equations are as follow:[3]

$$
\frac{\partial \overline{\rho}}{\partial t} + \frac{\partial \overline{\rho}\widetilde{u}_i}{\partial x_i} = 0
$$
$$
\frac{\partial \overline{\rho}\widetilde{u}_i}{\partial t} + \frac{\partial}{\partial x_j}\left[\overline{\rho}\widetilde{u}_i\widetilde{u}_j + \overline{p}\delta_{ij} - \overline{\tau_{ij}} + \tau_{ij}^{sgs}\right] = 0
$$
$$
\frac{\partial \overline{\rho}\widetilde{E}}{\partial t} + \frac{\partial}{\partial x_i}\left[\left(\overline{\rho}\widetilde{E} + \overline{p}\right)\widetilde{u}_i + \overline{q}_i - \widetilde{u}_j\overline{\tau_{ji}} + H_i^{sgs} + \sigma_i^{sgs}\right] = 0
$$

(1)

In the above equations, the species equations are not included, since in LEMLES they are solved using another approach and is not explicitly filtered as the rest of the conservation equations. Here, $\widetilde{u}_i$ is the i-th filtered velocity component, $\overline{p}$ is the filtered pressure that is computed from the filtered equation of state: $\overline{p} = \overline{\rho}R_u \sum_{k=1}^{n}\left(\frac{\widetilde{Y_k}\widetilde{T}}{W_k} + \frac{[\widetilde{Y_kT} - \widetilde{Y_k}\widetilde{T}]}{W_k}\right)$. If the subgrid temperature-species correlation is neglected (it has been found negligible in flows of current interest) then, $\overline{p} = \overline{\rho}R\widetilde{T}$. Here, R_u is the universal gas constant and R is the mixture gas constant. The total filtered energy is defined as $\widetilde{E} = e + \frac{1}{2}(\widetilde{u_k}^2 + k^{sgs})$, $k^{sgs} = \frac{1}{2}\left[\widetilde{u_k^2} - \widetilde{u_k}^2\right]$ is the subgrid kinetic energy and e is the internal energy given as the sum of the sensible enthalpy and the chemical stored energy as $e = \sum_{m=1}^{N} Y_m h_m - \frac{p}{\rho}$. The species enthalpy is calculated from the caloric equation of state: $h_m = \Delta h_{f,m}^0 + \int_{T_o}^{T} c_{p,m}(T)dT$. Also, $h_{f,m}^0$ is the standard heat of formation at standard state and $c_{p,m}$ is the specific heat at constant pressure for the mth species. The filtered viscous shear stress ($\overline{\tau_{ij}}$) and heat flux ($\overline{q}_i$) are approximated using the filtered velocity and temperature.

The filtered LES equations contain many subgrid terms that require closure. These terms represent the effect of the unresolved motion on the resolved field. The subgrid terms τ_{ij}^{sgs}, H_i^{sgs}, σ_i^{sgs} are respectively, the subgrid shear stress, the subgrid heat flux and the subgrid viscous stress. These terms are defined as:[3]

$$
\tau_{ij}^{sgs} = \overline{\rho}\left[\widetilde{u_iu_j} - \widetilde{u}_i\widetilde{u}_j\right]
$$
$$
H_i^{sgs} = \overline{\rho}\left[\widetilde{Eu_i} - \widetilde{E}\widetilde{u}_i\right] + \left[\overline{pu_i} - \overline{p}\widetilde{u}_i\right]
$$
$$
\sigma_i^{sgs} = \overline{u_j\tau_{ji}} - \widetilde{u}_j\overline{\tau_{ji}}
$$

(2)

The models for these subgrid terms are described in the next section.

A.   Subgrid closure for LES equations

The closure for the subgrid stresses and subgrid heat flux is achieved using an eddy viscosity model. Such a closure is acceptable since the small-scales primarily provide dissipation for the energy transferred from the large scales. The subgrid model used here is based on the solution of a transport equation for the subgrid kinetic energy, k^{sgs}. The ability of this model has been demonstrated and tested extensively in the past.[16, 17, 3, 18, 8, 19, 10]

The k^{sgs} transport equation model is given by:

$$
\frac{\partial \overline{\rho}k^{sgs}}{\partial t} + \frac{\partial}{\partial x_i}\left(\overline{\rho}\widetilde{u}_i k^{sgs}\right) = P^{sgs} - D^{sgs} + \frac{\partial}{\partial x_i}\left(\frac{\overline{\rho}\nu_T}{Pr_T}\frac{\partial k^{sgs}}{\partial x_i}\right)
$$

(3)

Here, Pr_T is a subgrid Prandtl number, assumed to be unity, and P^{sgs} and D^{sgs} represent respectively, the production and the dissipation of the subgrid kinetic energy. These terms are modeled as follow:

$$
P^{sgs} = -\tau_{ij}^{sgs}\frac{\partial \widetilde{u}_i}{\partial x_j}
$$

(4)

$$
D^{sgs} = C_\epsilon \overline{\rho}(k^{sgs})^{3/2}/\overline{\Delta}
$$

(5)

The subgrid shear stress and the subgrid heat flux using k^{sgs} model are modeled as:

$$
\tau_{ij}^{sgs} = -2\overline{\rho}\nu_T\left(\widetilde{S}_{ij} - \frac{1}{3}\widetilde{S}_{kk}\delta_{ij}\right) + \frac{2}{3}\overline{\rho}k^{sgs}\delta_{ij}
$$

(6)

American Institute of Aeronautics and Astronautics Paper 2005-3971

$$H_i^{sgs} = -\nu_T \frac{\partial \widetilde{h}}{\partial x_i} \tag{7}$$

where the subgrid eddy viscosity is given by $\nu_T = C_\nu (k^{sgs})^{1/2} \overline{\Delta}$. The subgrid viscous work $\sigma_i{}^{sgs}$ is neglected based on past studies. Here, $\overline{\Delta}$ is the grid filter width and $\widetilde{h}$ is the specific enthalpy.

The two model coefficients C_ϵ and C_ν must be prescribed or obtained dynamically as a part of the solution. Currently, these two coefficients are employed as constant values of $C_\nu = 0.067$ and $C_\epsilon = 0.916$, which were employed in recent studies as well.[7,8] However, a localized dynamic approach has been developed[17,3,18] that has resulted in a robust and stable way for determining the model coefficients locally in the combustor without requiring any averaging or smoothing. We plan to revisit the current study using this dynamic approach in the near future.

B.   Subgrid combustion model

Physically, scalar mixing, combustion and heat release occur at the small-scales, however, in conventional LES, the small-scales are not resolved. Therefore, modeling of these subgrid processes at the filtered level involve models that may not be applicable for all conditions.

In LEMLES, models at the resolved scales are avoided altogether. Instead, scalar evolution is modeled by a combined Eulerian-Lagrangian approach that captures both the large- and the small-scale processes correctly. All processes occurring below the LES grid scale, such as reaction-diffusion, heat release, volumetric expansion, and turbulent stirring by the small-scales (i.e., scales below the grid scale $\overline{\Delta}$) are simulated within each LES cells on a one-dimensional domain (the LEM domain). The large-scale transport (by the LES resolved mass transport) of the subgrid scalar fields across LES cells is modeled by a Lagrangian advection process that ensures exact mass conservation. Although details are given elsewhere,[7,8,12] we briefly summarize the key features, for completeness.

LEM is a stochastic subgrid model, which treats molecular diffusion and turbulent convection separately, but concurrently within a 1D domain. This 1D is not a physical direction, rather it is in the direction of the flame normal (in premixed) or maximum scalar gradient (in non-premixed). The resolution in the 1D domain can be made fine enough to resolve the Kolmogrove scale η. The reaction-diffusion equations and the subgrid energy equation in the 1D LEM domain are:[20]

$$\frac{\partial Y_k}{\partial t} = -\frac{1}{\rho} \frac{\partial \rho Y_k V_k}{\partial s} + \frac{\dot{\omega}_k W_k}{\rho} + F_{kstir} \tag{8}$$

$$\frac{\partial T}{\partial t} = -\frac{1}{\overline{C_p}} \sum_{k=1}^{N} C_{p,k} Y_k V_k \frac{\partial T}{\partial x} + \frac{1}{\rho \overline{C_p}} \frac{\partial}{\partial x} \left(\overline{\kappa} \frac{\partial T}{\partial x} \right) - \frac{1}{\rho \overline{C_p}} \sum_{k=1}^{n} h_k \omega_k W_k + F_{Tstir} \tag{9}$$

where the molecular diffusion is obtained from Fick's law:

$$V_k = -\frac{D_k}{Y_k} \frac{dY_k}{dx} \tag{10}$$

Since the small-scale turbulent stirring of the scalar fields is done explicitly, they are denoted as F_{kstir} and F_{Tstir} in the above equations. These terms are implemented using stochastic rearrangement events called triplet maps, each of which represents the action of a turbulent eddy on the scalar fields, as shown in Fig. 1. Stirring mimics the action of a single eddy on a scalar field. Three quantities govern the stirring event: the eddy size, location and the rate of stirring. The eddy size is sampled randomly from a PDF of eddy sizes given by $f(l)$ in the range $\eta < l < \Delta$:

$$f(l) = \left(\frac{5}{3} \right) \frac{l^{-8/3}}{\eta^{\frac{5}{3}} - \Delta^{\frac{5}{3}}} \tag{11}$$

This PDF is computed based on the inertial range scaling for 3D turbulence.[21,22] While the event location is randomly chosen from a uniform distribution within the 1D domain, the event rate is calculated as

$$\lambda = \frac{\nu Re}{C_\lambda \Delta^3} \frac{[\frac{\Delta}{\eta}]^{\frac{5}{3}} - 1}{1 - [\frac{\eta}{\Delta}]^{\frac{4}{3}}} \tag{12}$$

Where C_λ is a model constant taken as 5.0 in the current study.[20] The stirring time interval is given by $\Delta t_{stir} = 1/\lambda X_{LEM}$, where X_{LEM} is the length of the computational LEM domain, λ is the event frequency per unit length, and ν is the kinematic viscosity of the mixture. The Kolmogorov length scale η is determined by the inertial range scaling law, $\eta = N_\eta L Re^{-3/4}$. The Lagrangian transport of the subgrid scalar fields in the LES cells are then implemented based on global 3D mass flux by the resolved velocity field. More details are in the cited references.

In the current study, a global one-step mechanism for methane-air combustion[23] is used: $CH_4 + 2O_2 + 3.76N_2 \longrightarrow CO_2 + 2H_2O + 3.76N_2$ with a reaction rate is given by: $k = 2.4E16\,exp^{-24358.3/T}[CH_4][O_2]$. This five-species mechanism is not expected to capture all the features seen in the experiment but should be reasonable to predict the global features, especially the effect of heat release on the velocity field. We plan to revisit this test case with a more general reaction mechanism in the near future.
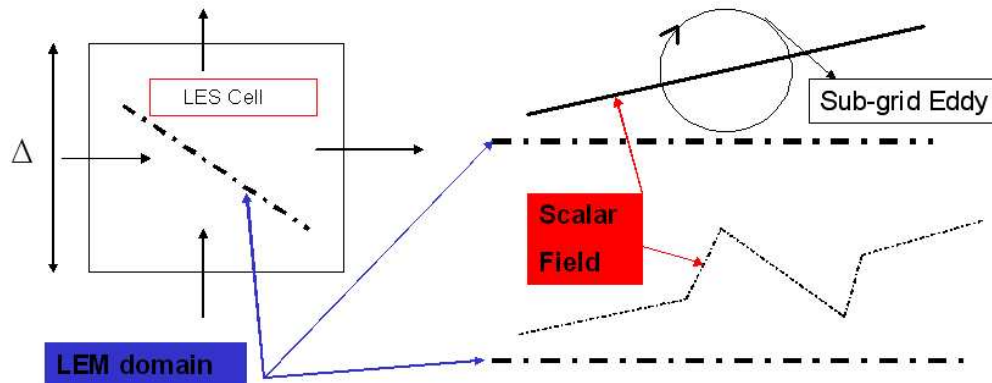

Figure 1. The LEM domain inside the LES cell and the triplet mapping effect on the subgrid domain

III.   Configuration and Setup

Figures 2 (a-c) show respectively, the Sydney swirl burner,[13] a schematic of the computational domain simulated in the current study and a representative grid distribution. The burner has a bluff body of diameter $50mm$ with a central $3.6mm$ diameter fuel injector. The primary air flow stream is injected from an annulus that surrounds the bluff body, with an outer diameter of $60mm$. The blockage ratio, $\left(2r_b^2/2r_s^2\right)$, is equal to 0.69 where r_s is the outer radius of the annulus and r_b is the bluff body radius.[24] The burner assembly is placed in a SNL wind tunnel with a square cross sectional area of 305 x $305mm$. The wind tunnel provides a secondary air co-flow with a free stream turbulence level of 2%.

Ideally, the LES should include the entire swirl burner assembly in order to capture the proper inflow into the combustor. However, this is an expensive approach and is not adopted at present, Instead, as shown in the schematic diagram in Fig. 2(b), the simulation starts at the injector outlet cross section. This does require effort to determine the inlet velocity profiles since data is only available around 6.8 mm downstream of this inlet plane. Profiles at the inlet were adjusted to match the global flow rate and also the near field profiles at 6.8 mm as best as possible.

The combustor computational domain is 210 mm length with 305mm x 305 mm cross sectional area. Thus, in this study, the complete SNL wind tunnel facility is included in the computational domain. A two-domain butterfly type grid approach is used in the current study. The region near the centerline is resolved using a Cartesian grid to avoid the singularity in the cylindrical grid, while the rest of the domain is resolved over a cylindrical grid. The inner Cartesian grid resolution is 210 X 38 X 38 in the axial, horizontal and vertical directions, while the outer cylindrical grid is 210x110x153 points in the axial, radial and circumferential directions. We employ the same grid for both the cold and the hot flow test cases. The grid is clustered in the regions of high shear, especially in the swirling annular flow. It is estimated that shear layer is resolved by over 10 points, which is considered reasonable. The fuel injector, which is 3.6 mm in diameter is located inside

the central Cartesian grid and therefore, is only resolved in an approximate manner. However, approximately 38x38 grid points are present in the injector diameter and therefore, the jet evolves quite well within a few mm from the exit plane and becomes circular very quickly. At this time, any error due to this resolution of the jet has not been addressed, but as the results described below show, this is not a major issue.

For the LEMLES reacting flow case, a representative 9 LEM cells are used within each LES cell. This is considered rather coarse and is not sufficient to resolve all the small scales within the LES cells. Estimate of the local subgrid Reynolds number shows that typically in the regions of high turbulence, the Kolmogorov scale is around 0.014 mm, whereas, the typical grid scale is around 0.05 mm. Thus, the subgrid LEM resolution is only capable of resolving only eddies just below the grid scale $\overline{\Delta}$. Nevertheless, we believe this study offers a first ever evaluation of this complex flame case using the LEMLES approach that captures both the large and small-scale features accurately.

The flow conditions are extracted from the Sydney university web-page[25] for swirl and bluff body stabilized flame configurations. Table 1 shows the different inflow parameters for the both cold and hot test cases.[24]

Flow Case	Jet	S_g	U_j	U_s	U_e	Re
N29S054	Air	0.54	66	29.74	20.0	59000
SM1	CH_4	0.5	32.7	38.2	20.0	76000

Table 1: Cold and hot flow test case parameters

Here, U_j is the central jet velocity, U_s is the axial velocity component of the primary air flow, U_e is the secondary axial wind tunnel co-flow velocity and Re is the Reynolds number. The geometrical swirl number S_g is defined as the ratio of the mean bulk tangential to axial velocity coming from the swirl annulus,[13] $S_g = \frac{\overline{W_s}}{\overline{U_s}}$. The flow swirl number S is defined as the ratio between the axial flux of swirl momentum divided by the the axial flux of axial momentum[26] as follow:

$$S = \frac{\int_0^R \rho u_x W_\theta r^2 dr}{R \int_0^R \rho U_x U_x r} \tag{13}$$

For the flow conditions reported here, a value of $S = 0.61$ is obtained. This value is close to the critical swirl number (typically around 0.6) and therefore, is high enough to create the classical vortex breakdown bubble[27] downstream of the dump plane. For the reacting case, this bubble, along with the base recirculation zones are expected to provide the stabilizing mechanism for the flame, as discussed later.

THE LEMLES solver used here is a finite volume scheme that is second order accurate in space and time. A fourth order accurate spatial scheme is also available but has not been used here. Inflow and outflow boundary conditions are prescribed using characteristic conditions,[28] and no-slip, non-catalytic adiabatic conditions are used at all walls. A 2 percent of turbulence is also added at the inflow, however, this is done rather arbitrarily since no data is available about the actual conditions at the inflow.

IV.   Non-Reacting Flow Results

The cold flow test case has been compared to the experimental results provided at the Sydney University website.[25] In all the following figures, the black dots correspond to the LDV experimental data and the solid lines are the LES results. Typically, LES results are averaged over 6 flow through times after the initial transients.

Analysis of the instantaneous axial velocity field shows that the bluff body creates a recirculation zone (RZ) just downstream of the dump plane. The size of the RZ is approximately the half-width of the dump plane and is located just above the central jet. Visualization of the flow in this near-field shows that the 3D structure of this RZ is in the form of toroid that stabilizes nearly one bluff body diameter downstream of the burner face (approximately 40 mm). This result agrees very well with the experiment data.[29] The shear flow around this RZ accelerates and converged toward the centerline and meets with the central fuel jet (in the cold flow case, only air is injected). Enhanced mixing is expected to occur due to this flow convergence.

A detailed comparison for LES velocity fields has been performed for this test case. In general, the LES predictions of the time-averaged size, location and intensity of the recirculation zone are in excellent agreement with data.[30] The overall time-averaged flow features show that there are two regions of recirculation.

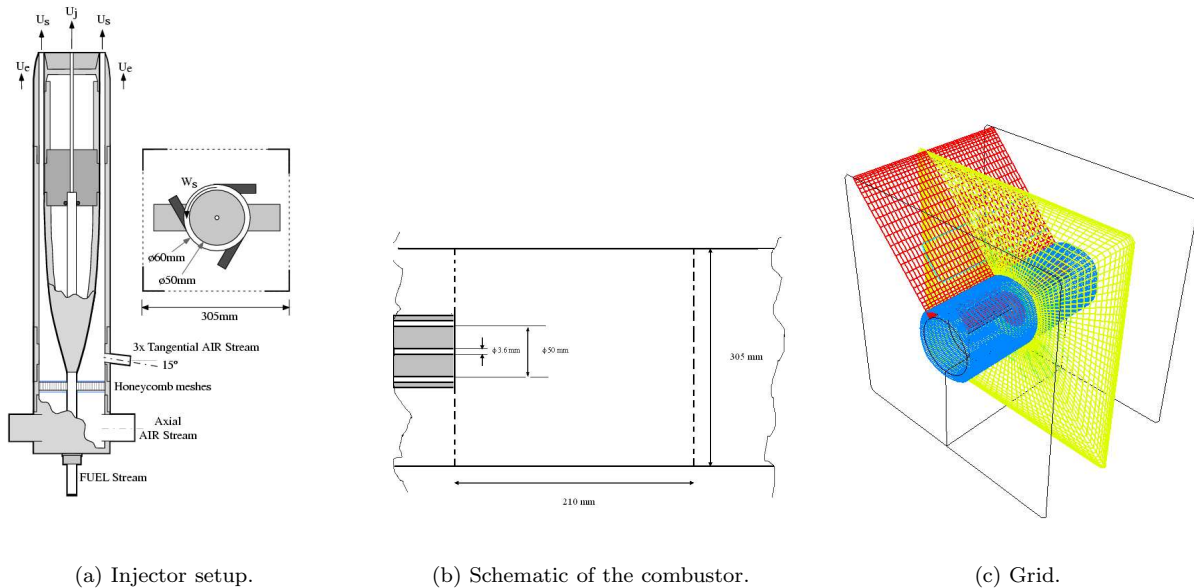(a) Injector setup.　　　　　(b) Schematic of the combustor.　　　　　(c) Grid.

Figure 2. The Swirl injector, computational domain and grid

A region close to the bluff body contains the afore-mentioned RZ reverse flow (around 25 mm) and another region further downstream, approximately between $x = 58$ mm and $x = 100$ mm that is more representative of the vortex breakdown bubble (VBB) associated with swirl flow.[30]

Figure 3 shows the time-averaged, axial velocity vector plot at two locations: (a) just downstream of the bluff body and (b) downstream near the VBB. It can be seen in Fig. 3(a) that the primary bluff-body RZ is located approximately one diameter downstream of the dump plane and is located above the central jet. The counter-clockwise recirculation caused by the toroidal RZ interacts with the primary fuel jet and causes significant increase in the spreading of this jet. As noted earlier, this flow dynamics is likely to enhance mixing between the fuel and oxidizer.

Figure 3(b) shows the near field of the VBB region that occurs further downstream. It can be seen that this VBB is an elongated structure approximately 44 mm in axial extent at the centerline but with a width approximately 10 mm at this central plane. 3D flow visualization shows that this structure is 13 mm in the spanwise direction.

Figure 4 shows the iso-surface for the axial vorticity component. As is expected in high Reynolds number flow, a wide range of scales in turbulent structures are created in this flow field. In the dump plane near-field, the structures are more coherent but they quickly break down further downstream of the VBB into more randomly oriented small scale structures.

Direct comparison with data is also carried out to demonstrate the accuracy of the LES approach. The centerline mean axial velocity is shown in Fig. 5. The leading and trailing stagnation point locations that represent the extent of the VBB, and the axial centerline velocity decay are captured accurately. The centerline axial velocity decays first due to jet spreading, and then further downstream, the velocity increases again under the effect of entrainment of the co-flow.[29] Slight deviation from the measured values in the far field may be a result of coarser grid in that region.

The radial time-averaged mean axial, azimuthal and radial velocity profiles at the first four upstream locations locations (between 6.8 mm and 40 mm) are shown in Figs. 6(a)-(c), respectively. The corresponding velocity profiles in the region 50 mm to 125 mm (downstream of the VBB) are shown in Figs. 7(a)-(c). In the near-field, the mean axial velocity shows a peak around R = 28 mm in the shear layer generated between the primary and secondary flow field. This peak decays axially as the shear layer spreads such that by around 70 mm there is no longer any discernible peak. The azimuthal velocity component peaks at $x = 40$ mm due to the formation of the highly rotational collar-like structures.

Overall there is excellent agreement with the measured data.[29] Slight deviations are noted at the locations

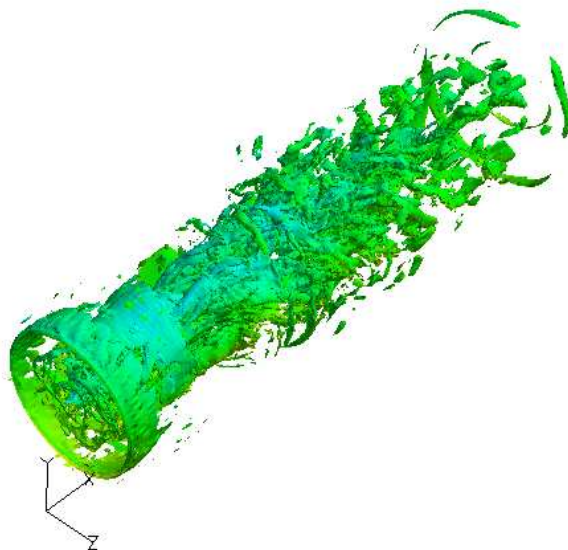American Institute of Aeronautics and Astronautics Paper 2005-3971
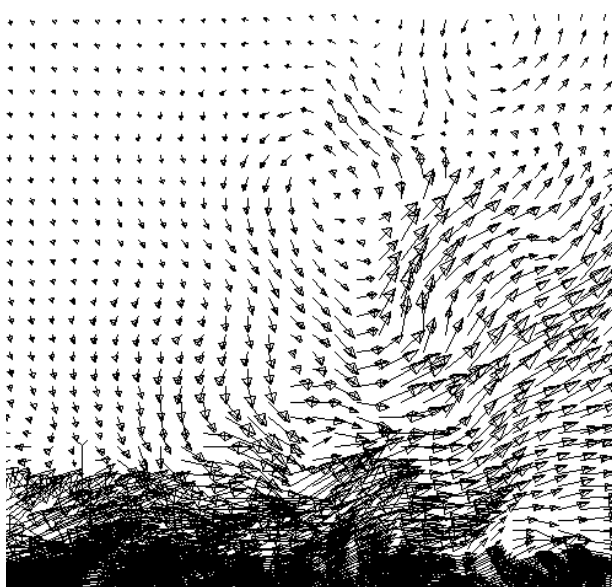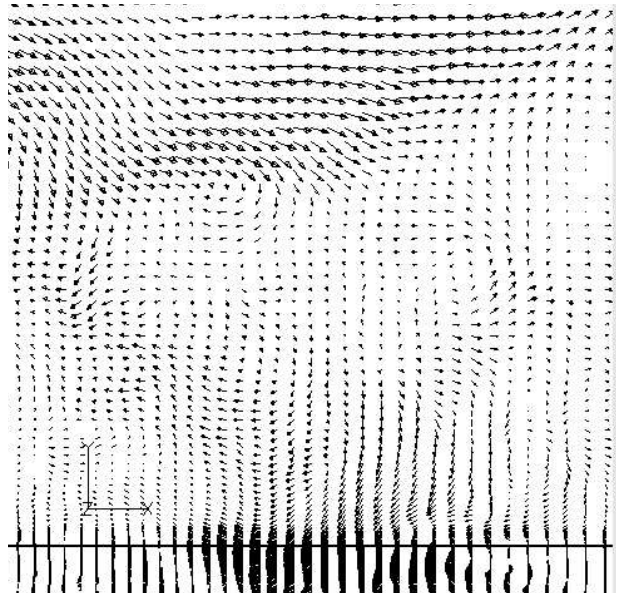
(a) Vector plot for RZ.

(b) Vector plot for RB at the centerline.

Figure 3. Velocity vector plot in the x-y central plane
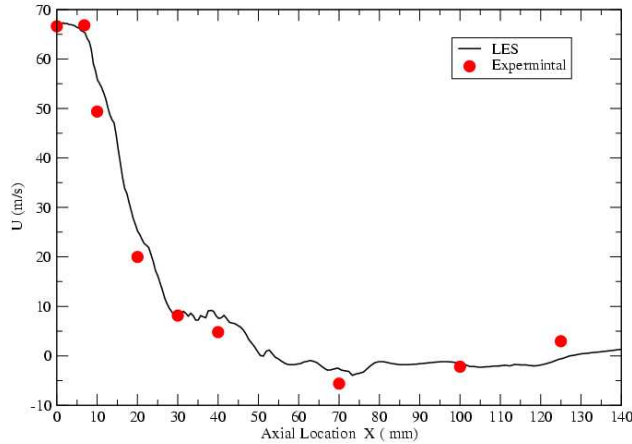

Figure 4. Mean axial vorticity iso-surface

American Institute of Aeronautics and Astronautics Paper 2005-3971

Figure 5. Centerline mean axial velocity profile

of maximum shear and near the centerline. A plausible explanation for this is that the inflow conditions are approximated here due to lack of upstream information. For instance, the flow inside the swirl vanes and the inflow pipe should be simulated to simulate the correct inflow profiles (which includes both the mean and fluctuating components) at $x = 0.0$ section. However, this is not attempted in the current study. The ambiguity in the inflow specification is also reflected in the RMS profiles as well. Nevertheless, the current LES shows an ability to capture the mean and RMS velocity components accurately, given all the uncertainties regarding the inflow.

(a) $\overline{U_x}$(m/sec). (b) $\overline{W_\theta}$(m/sec). (c) $\overline{V_r}$(m/sec).
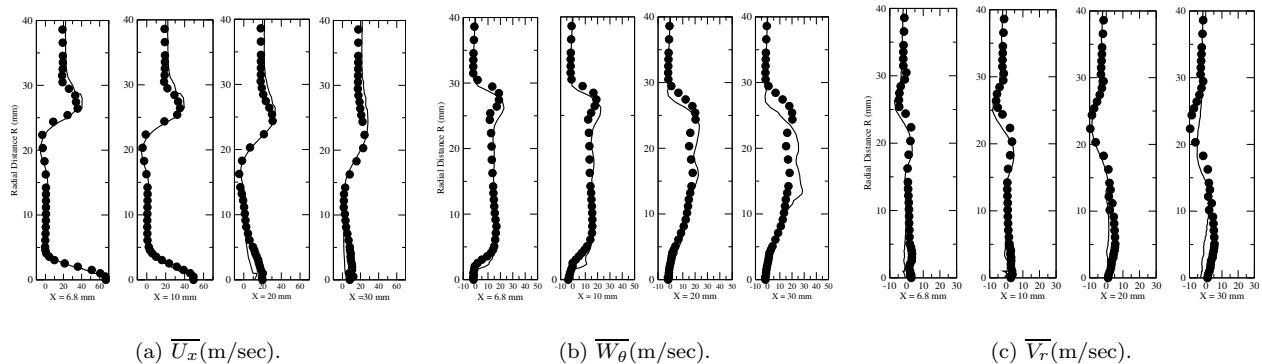
Figure 6. Radial mean velocity profiles, (LDV -•-, LES −) at $x = 6.8$mm, 10 mm, 20 mm and 30 mm

The three-component root-mean-square (RMS) velocity fluctuation radial profiles at the first four upstream locations are shown in Fig. 8. Good agreement is achieved overall. The axial component shows a bimodal behavior at the location $x = 6.8$ mm. The tangential and azimuthal components also show two peaks, one at the centerline and another in the shear layer region at the outer edge of the bluff body.

Figure 9 shows the downstream locations for the RMS velocity components. No significant change is observed other than the increase in the rotational velocity between $x = 40$ mm and 125 mm at the centerline due to the existence of the VBB. There is some discrepancy in the peak value in the centerline region but overall, the agreement is considered acceptable.

An encouraging aspect of this cold flow LES study is that many of the finer details typically needed for LES inflow setup (inflow turbulence spectrum, turbulence profiles, etc.) may not be that important (at least for this setup) since most of the features are captured with reasonable accuracy without this knowledge, as demonstrated in the above figures.
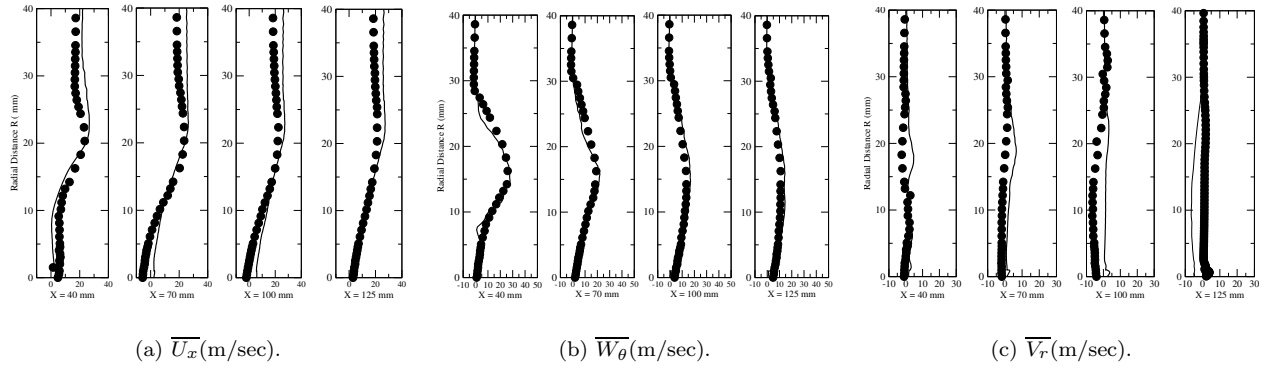
American Institute of Aeronautics and Astronautics Paper 2005-3971

(a) $\overline{U_x}$(m/sec).

(b) $\overline{W_\theta}$(m/sec).

(c) $\overline{V_r}$(m/sec).

Figure 7. Radial mean velocity profiles, (LDV -•-, LES −) at $x = 40$mm, 70 mm, 100 mm and 125 mm

(a) U_{rms}(m/sec).

(b) $W_\theta rms$(m/sec).

(c) $V_r rms$(m/sec).
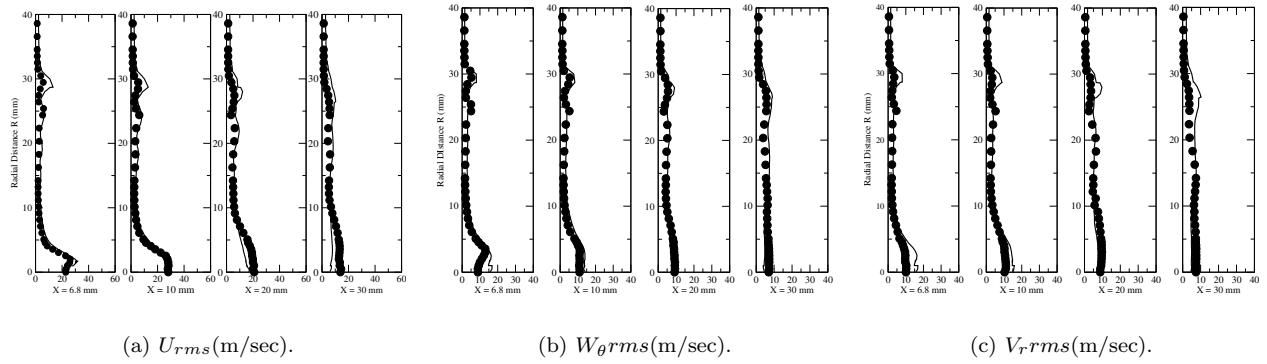
Figure 8. Radial RMS velocity profiles, (LDV -•-, LES −) at $x = 6.8$mm, 10 mm, 20 mm and 30 mm

(a) U_{rms}(m/sec).

(b) $W_\theta rms$(m/sec).

(c) $V_r rms$(m/sec).
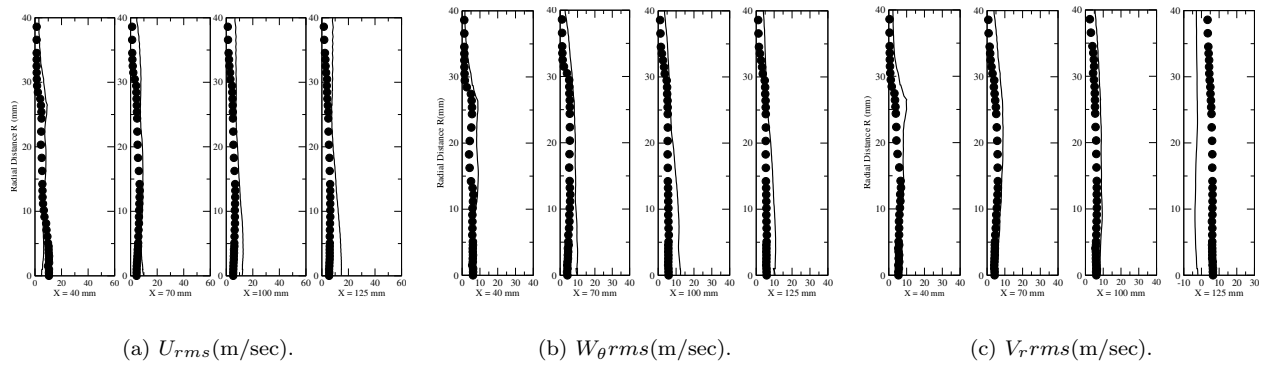
Figure 9. Radial RMS velocity profiles, (LDV -•-, LES −) at $x = 40$mm, 70 mm, 100 mm and 125 mm

American Institute of Aeronautics and Astronautics Paper 2005-3971

V.   Reacting Flow Results

The LIF and LDV data extracted from[25] are compared here to the LESLEM results for the reacting case. Figure 10 (a) shows the instantaneous contours for axial velocity component. A toroidal recirculation zone close to the bluff body is again established. Also, a second recirculation zone, characteristic of the VBB is also observed downstream, around $x = 120$ mm. These results agree well with the experimental data, which states that flame SM1 has two recirculation zones.[24] Figure 10 (b) shows the contours for the rotational velocity component in the center x-y plane. A high rotational velocity collar-like structure is observed in-between the two recirculation zones. As the axial velocity decays axially, the rotational velocity increases by the conservation of momentum. The flame shows necking behavior at this location, which was also observed by Kalt et al.[31]

(a) Axial velocity contours   (b) Azimuthal velocity contours
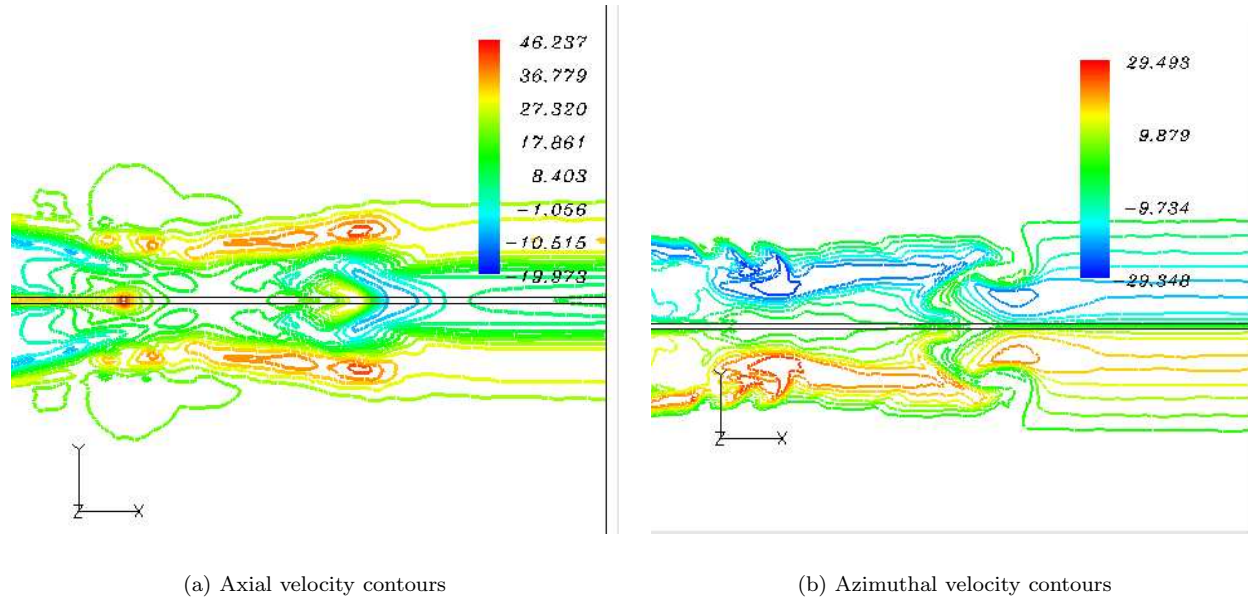
Figure 10. Instantaneous velocity contours in the $x - y$ center plane for the SM1 flame.

Figure 11 shows the instantaneous contours of temperature (colored) and CH_4 mass fraction (black). The flame type features here are the same as the H-type mentioned in the experiments.[24, 13] LES-LEM predicts a flame length of 111 cm, which is comparable to the 120 mm mentioned by Masri et al.[13] The flame also shows necking around 63 mm. The necking area corresponds to location of maximum interaction between turbulence and chemistry. At such locations, the turbulence time scale is comparable to the chemistry time scale. If the swirl number is increased further, the flame is expected to become extinct at the neck location or finally lift-off.

Figures 12(a) and (b) show respectively, the radial mean temperature profiles at different axial locations and the centerline variation in the axial direction. At locations $x = 10$ mm and $x = 20$ mm, which are inside the first recirculation zone near the bluff body, the temperature peaks at the outer edges of the bluff body location. These regions are in the shear layer and at these locations the shear stress is expected to be high and turbulence combustion interaction is very effective. The mixing of the recirculating products with the incoming reactants increases the combustion efficiency, and hence increases the temperature locally. As we go further downstream, the shear layer spreads and the temperature goes down in the shear layer region. The peak moves toward the centerline as the flame necks. A peak near the centerline is seen around $x = 75$ mm, which is in the location of the second recirculation zone. Along the centerline, the temperature in the cold fuel jet is somewhat under predicted but the overall the increase in the temperature and then the far field decay seems reasonable. As noted earlier, we are employing a one-step global kinetics model and there are some inherent limitation of this simplified closure. Nevertheless, the overall agreement is encouraging.

Figure 13 shows comparison between the data and the centerline velocity for both the hot flow and the cold flow test cases. For the velocity field overall good agreement is observed for the hot flow (the cold flow result is discussed earlier). The second recirculation bubble (i.e., VBB) is seen between $x = 80$ mm and x
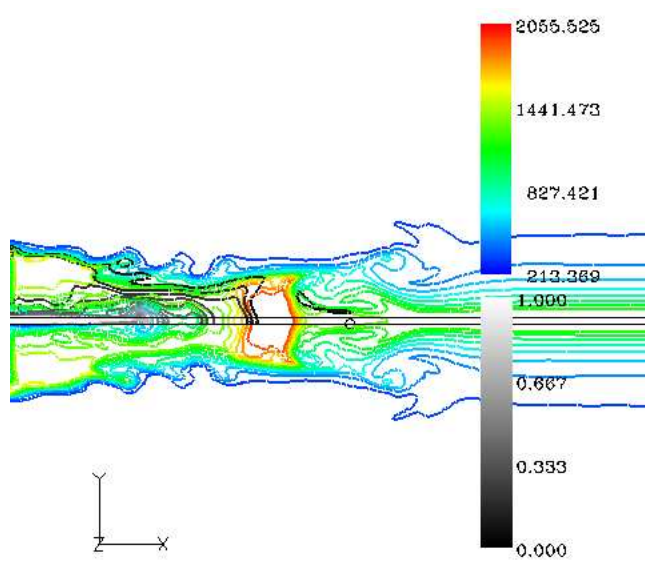
Figure 11. Instantaneous temperature contours and Y_{CH_4} (black lines) for the SM1 flame.

$= 100$ mm for the hot flow case. In contrast, the cold flow VBB occurs between 60 mm and 100 mm and is longer, with peak negative velocity much smaller than in the hot flow case. The second recirculation zone is predicted slightly smaller than the experimental result.
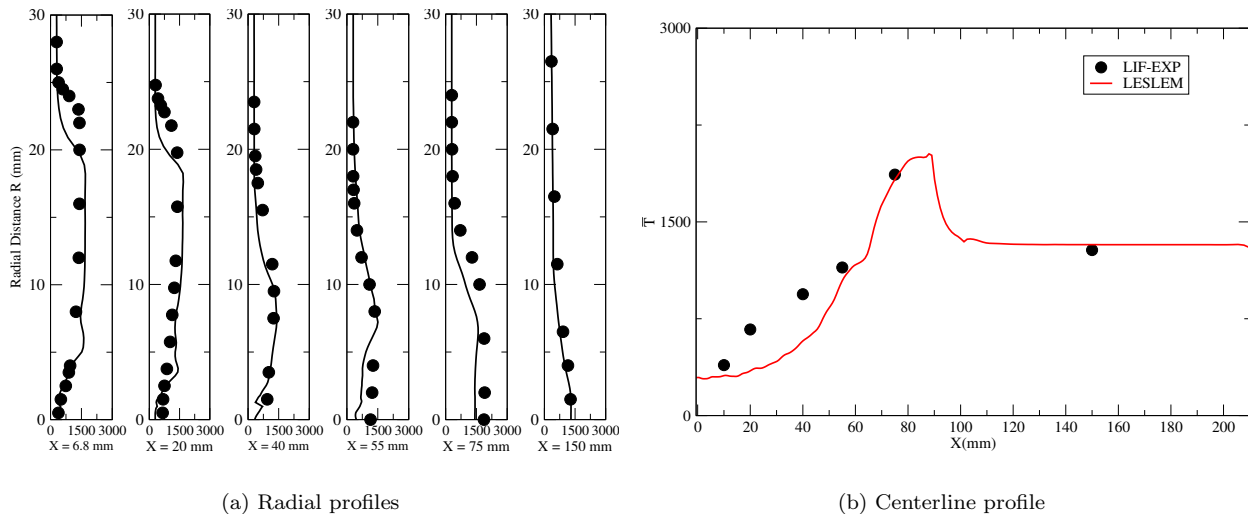

(a) Radial profiles

(b) Centerline profile

Figure 12. Mean temperature radial profile $\overline{T}$(LIF -•-, LESLEM --) at various axial location and centerline variation for the SM1 flame.

Figures 14(a) and (b) show respectively, the close-up velocity vector field near the two recirculation zones for the SM1 flame case. As noted earlier, the RZ near the bluff body acts as a toroidal structure and is located around one bluff body diameter downstream of the dump plane. The VBB which occurs further downstream is more compact (when compared to the cold flow) but with larger negative velocities inside the bubble region.

Figures 15(a) and (b) show respectively, the mean axial and the mean azimuthal velocity components for flame SM1. Excellent agreement is achieved except for slight deviation at the center line location. Again, the axial velocity rapid deceleration in the axial direction reflects formation of a toroidal shape recirculation zone just downstream of the bluff body, and another recirculation zone concentrated at the centerline downstream
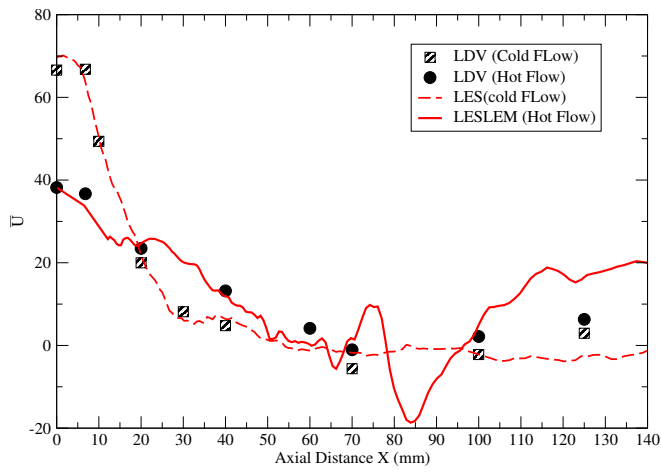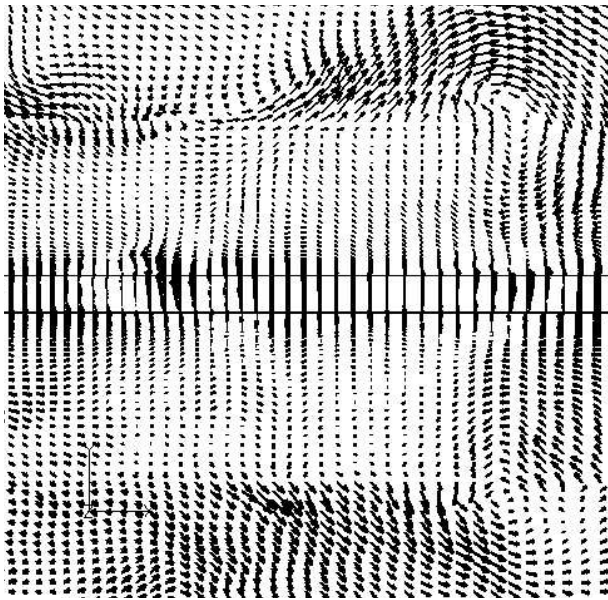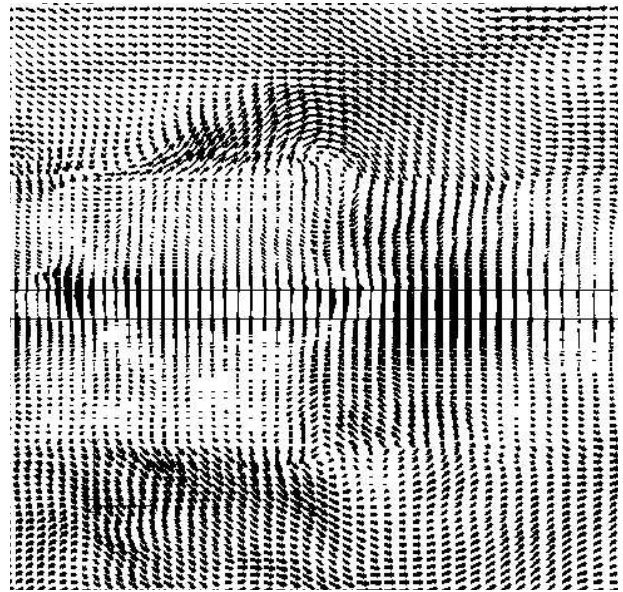
American Institute of Aeronautics and Astronautics Paper 2005-3971

Figure 13. Mean centerline axial velocity profile $\overline{U}$(LDV -•-, LESLEM (SM1 flame), LES — (cold flow)).

(a) RZ near the bluff body

(b) VBB along the centerline

Figure 14. Velocity vector field for the SM1 flame in the $x-y$ center plane.

American Institute of Aeronautics and Astronautics Paper 2005-3971

of the jet. The azimuthal velocity increases significantly between $x = 60$ mm and $x = 70$ mm, where the rotating collar-like structures are formed.

Figures 16(a) and (b) show respectively, the radial profiles of the RMS values for the axial and the azimuthal velocity at various axial locations. Overall, good agreement is achieved at the near-inflow locations. The far field may need more run time to settle down. The RMS values show a peak near the edge of the bluff body especially at the first few locations, indicating the presence of the shear layer.

Finally, Figs. 17(a) and (b) show respectively, the radial profiles for the mean mass fractions of H_2O and CO_2 at different axial locations. Considering that a single-step global kinetics is employed in the LEMLES, the overall agreement is encouraging. However, there are regions of deviation, for example, near the centerline at $x = 55$ mm location, where the flame necking exists. In addition, under prediction is observed at the corner of the bluff body at the 6.8 mm location. This trend follow generally the mean temperature behavior as well. The deviation from the experimental results is attributed to the usage of a single step mechanism. Nevertheless, LEM shows excellent capability to predict the flame features and the turbulence chemistry interaction in this type of flame.
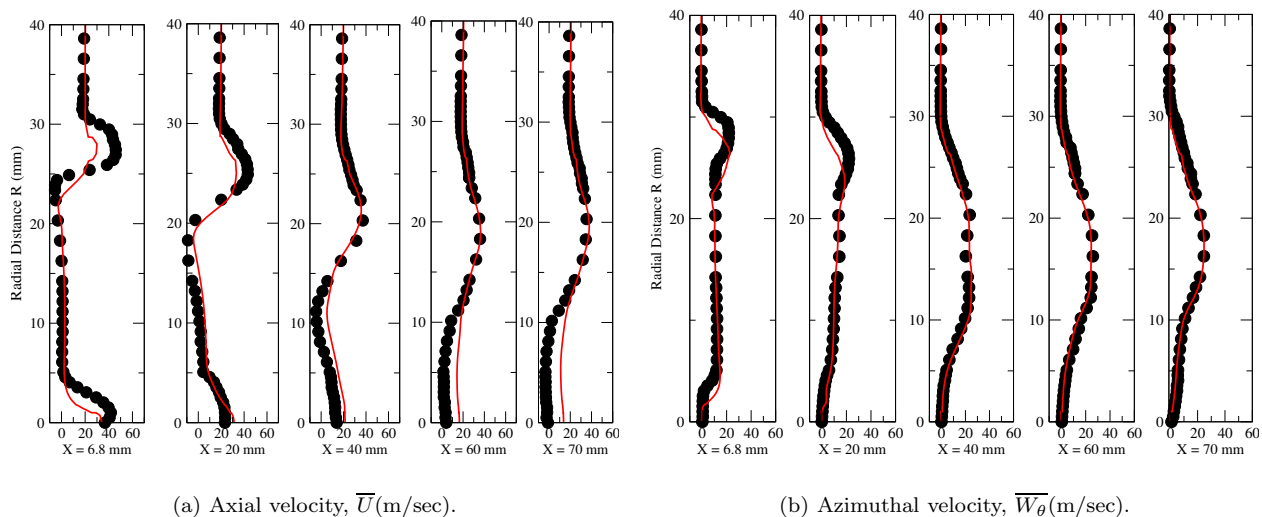

(a) Axial velocity, $\overline{U}$(m/sec).

(b) Azimuthal velocity, $\overline{W_\theta}$(m/sec).

Figure 15. Mean velocity profiles (LIF-LDV -•-, LESLEM −) for the SM1 flame.

(a) Axial RMS, U_{rms}(m/sec).

(b) Azimuthal RMS, $W_\theta rms$(m/sec).
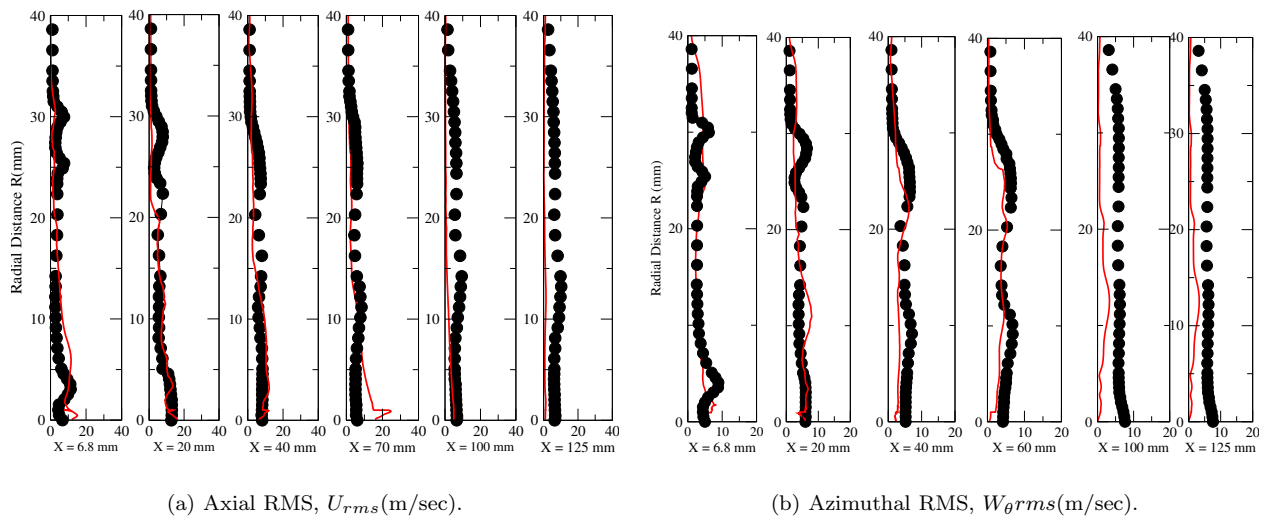
Figure 16. RMS velocity profiles (LIF-LDV -•-, LESLEM −) for the SM1 flame.

American Institute of Aeronautics and Astronautics Paper 2005-3971

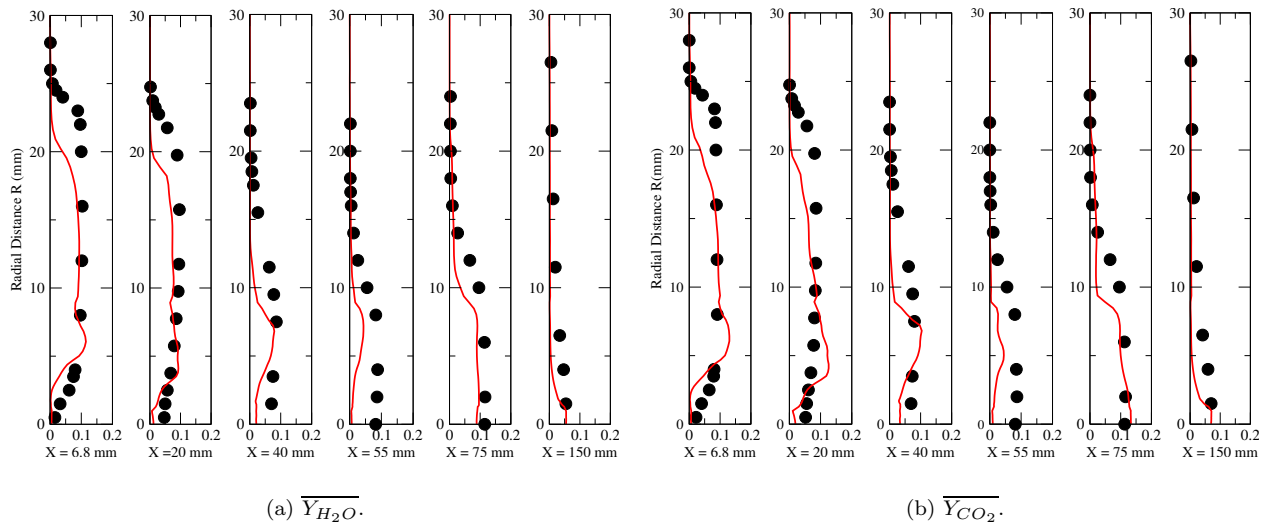(a) $\overline{Y_{H_2O}}$.   (b) $\overline{Y_{CO_2}}$.

Figure 17. Mean mass fraction profiles (LIF-LDV -•-, LESLEM −) for the SM1 flame.

VI.   Conclusion

In this study, a swirling bluff-body stabilized non-premixed flame experimentally studied at SNL has been simulated using LES. Both cold and hot flow cases are simulated and compared to data. For the hot flow study, the LEMLES based subgrid closure is employed using a simple one-step global kinetics in the subgrid. As shown, excellent agreement is achieved for the cold flow and for the hot flow in most properties compared. LESLEM shows good capability to predict the effect of heat release on the velocity field and also on the temperature field. Some deviations observed are attributed to the simplified chemistry employed here. The simulations also captured the characteristic features of this bluff-body stabilized swirling flame. Two recirculation zones are seen in both cold and hot flow. The first zone is toroidal swirling recirculation zone associated with the flow separation from the corners of the bluff body and is located approximately one diameter downstream of the dump plane. The second recirculation zone is like classical VBB seen in swirling flow and is located further downstream around the centerline. The size of this bubble shrinks with heat release. The flame is contained inbetween the recirculation zones with a neck region at the end of the first recirculation zone. All these observations are in excellent agreement with measured data.

These studies have clearly established the ability and accuracy of the LEMLES, considering that many inflow details were not available. Future studies may attempt the other swirl flames in the SNL data base and may also re-visit this case with a more detailed multi-step kinetics.

VII.   Acknowledgments

References

[1]Forkel, H. and Janicka, J., "Large-Eddy Simulation of a Turbulent Hydrogen Diffusion Flame," *Flow, Turbulence and Combustion*, Vol. 65, No. 2, 2000, pp. 163–175.

[2]Menon, S. and Calhoon, W., "Subgrid Mixing and Molecular Transport Modeling for Large-Eddy Simulations of Turbulent Reacting Flows," *Proceedings of the Combustion Institute*, Vol. 26, 1996, pp. 59–66.

[3]Kim, W.-W., Menon, S., and Mongia, H. C., "Large-Eddy Simulation of a Gas Turbine Combustor Flow," *Combustion Science and Technology*, Vol. 143, 1999, pp. 25–62.

[4]Wang, S. and Yang, V., "Unsteady flow evolution in swirl injectors with radial entry. II. External exitations," *Physics of Fluids*, Vol. 17, No. 045107, 2005, pp. 1–12.

[5]Chakravarthy, V. and Menon, S., "Linear-Eddy Simulations of Reynolds and Schmidt Number Dependencies in Turbulent

American Institute of Aeronautics and Astronautics Paper 2005-3971

Scalar Mixing," *Physics of Fluids*, Vol. 13, 2001, pp. 488–499.

[6]Sankaran, V. and Menon, S., "LES of Scalar Mixing in Supersonic Shear Layers," *Proceedings of the Combustion Institute*, Vol. 30, 2004.

[7]Chakravarthy, V. and Menon, S., "Large-Eddy Simulations of Turbulent Premixed Flames in the Flamelet Regime," *Combustion Science and Technology*, Vol. 162, 2000, pp. 175–222.

[8]Chakravarthy, V. and Menon, S., "Subgrid Modeling of Premixed Flames in the Flamelet Regime," *Flow, Turbulance and Combustion*, Vol. 65, 2000, pp. 23–45.

[9]Sankaran, V. and Menon, S., "Subgrid Combustion Modeling of 3-D Premixed Flames in the Thin-Reaction-Zone Regime," *Proceedings of the Combustion Institute*, Vol. 30, 2004.

[10]Eggenspieler, G. and Menon, S., "Numerical Simulation of Flame Extinction un the Broken-Reaction Zone Regime," AIAA-2006 (submitted).

[11]Menon, S., Sankaran, V., and Stone, C., "Dynamics of Swirling Premixed and Spray Flames," *AIAA 2001-1092*, 2001.

[12]Menon, S. and Sankaran, V., "Subgrid Combustion Modeling of Two-Phase Reacting Flows," *IUTAM Symposium on Turbulent Mixing and Combustion*, Kluwer Press, 2001, pp. 415–425.

[13]Masri, A.R.and Kalt, P. and Barlow, R., "The Compositional Structure of Swirl-Stabilized Turbulent Nonpremixed Flame," *Combustion and Flame*, Vol. 137, 2004, pp. 1 – 37.

[14]Masri, A., Pope, S., and Dally, B. B., "Propability Density Function Computations of a Strongly Swirling Nonpremixed Flame Stabilized on a New Burner," *Proceedings of the Combustion Institute*, Vol. 28, 2000, pp. 123 – 131.

[15]Erlebacher, G., Hussaini, M. Y., Speziale, C. G., and Zang, T. A., "Toward the Large-Eddy Simulation of Compressible Turbulent Flows," *Journal of Fluid Mechanics*, Vol. 238, 1992, pp. 155–185.

[16]Menon, S., Yeung, P.-K., and Kim, W.-W., "Effect of Subgrid Models on the Computed Interscale Energy Transfer in Isotropic Turbulence," *Computers and Fluids*, Vol. 25, No. 2, 1996, pp. 165–180.

[17]Kim, W.-W. and Menon, S., "A New Incompressible Solver for Large-Eddy Simulations," *International Journal of Numerical Fluid Mechanics*, Vol. 31, 1999, pp. 983–1017.

[18]Kim, W.-W. and Menon, S., "Numerical Simulations of Turbulent Premixed Flames in the Thin-Reaction-Zones Regime," *Combustion Science and Technology*, Vol. 160, 2000, pp. 119–150.

[19]Sankaran, V. and Menon, S., "Alignment Statistics and Small-Scale Structures in Swirling Spray Combustion," *Proceedings of the Combustion Institute*, Vol. 29, 2002, pp. 577–584.

[20]Sankaran, V. and Menon, S., "The Structure of Premixed Flame in the Thin-Reaction-Zones Regime," *Proceedings of the Combustion Institute*, Vol. 28, 2000, pp. 203–210.

[21]Kerstein, A. R., "Linear-Eddy Model of turbulent Scalar Transport and Mixing," *Combustion Science and Technology*, Vol. 60, 1988, pp. 391–421.

[22]Kerstein, A. R., "Linear-Eddy Model of Turbulent Transport II," *Combustion and Flame*, Vol. 75, 1989, pp. 397–413.

[23]Westbrook, C. K. and Dryer, F. L., "Simplified Reaction Mechanisms for the Oxidation of Hydrocarbon Fuels in Flames," *Combustion Science and Technology*, Vol. 27, 1981, pp. 31–43.

[24]Al-Abdeli, Y. M. and Masri, A., "Stability characteristics and flowfields of turbulent non-premixed swirling flames," *Combustion theory and Modeling*, Vol. 7, 2003, pp. 731 – 766.

[25]*Swirl Flame Web Database, http://www.aeromech.usyd.edu.au/thermofluids/swirl.html*, University of Sydney, 2005.

[26]Lilley, G., "Swirl Flows in Combustion: A Review," *AIAA Journal*, Vol. 15, No. 8, 1977, pp. 1063–1078.

[27]Syred, N. and Beer, J. M., "Combustion in Swirling Flows," *Combustion and FLame*, Vol. 23, 1974, pp. 143–201.

[28]Poinsot, T. and Lele, S., "Boundary Conditions for Direct Simulations of Compressible Viscous Flow," *Journal of Computational Physics*, Vol. 101, 1992, pp. 104–129.

[29]Al-Abdeli, Y. M. and Masri, A., "Precession and Recirculation in Turbulent Swirling Isothermal Jets," *Combust. Sci. Technol.*, Vol. 176, No. 5-6, 2004, pp. 645 – 664.

[30]Al-Abdeli, Y. M. and Masri, A., "Recirculation and Flowfield regimes of unconfined non-reacting swirling flows," *Exp. Therm. Fluid. Scien.*, Vol. 27, 2003, pp. 655 – 665.

[31]Kalt, P. A. M., Al-Abdeli, Y. M., Masri, A. R., and Barlow, R. S., "Swirling Turbulent Non-Premixed FLames of Methane: FLow Field and Compositional Structure," *Twenty-nine Symposium (International) on Combustion*, 2002, pp. 1913–1919.